

Leveraging both Lesion Features and Procedural Bias in Neuroimaging: An Dual-Task Split dynamics of inverse scale space

Xinwei Sun ^{*}, Wenjing Han[†], Lingjing Hu [†], Yuan Yao [‡], Yizhou Wang [§]

^{*}Microsoft Research Asia xinsun@microsoft.com

[†]Yanjiang Medical College, Capital Medical University {hanwj2014,hulj}@ccmu.edu.cn

[‡]Hong Kong University of Science and Technology. yuany@ust.hk

[§]Center on Frontiers of Computing Studies, Adv. Inst. of Info. Tech, Dept. of Computer Science, Peking University Yizhou.Wang@pku.edu.cn

Abstract—The prediction and selection of lesion features are two important tasks in voxel-based neuroimage analysis. Existing multivariate learning models take two tasks equivalently and optimize simultaneously. However, in addition to lesion features, we observe that there is another type of features, which are commonly introduced during the procedure of preprocessing steps, can improve the prediction result. We call such a type of features as *procedural bias*. Therefore, in this paper, we propose that the features/voxels in neuroimage data are consist of three orthogonal parts: lesion features, procedural bias and null features. To stably select lesion features and leverage procedural bias into prediction, we propose an iterative algorithm (termed GSplit LBI) as discretization of differential inclusion of inverse scale space, which is the combination of *Variable Splitting scheme* and *Linearized Bregman Iteration (LBI)*. Specifically, with a variable splitting term, two estimators are introduced and split apart, i.e. one is for feature selection (the sparse estimator) and the other is for prediction (the dense estimator). Implemented with Linearized Bregman Iteration (LBI), the solution path of both estimators can be returned with different sparsity level on the sparse estimator for selection of lesion features. Besides, the dense estimator can additionally leverage procedural bias to further improve prediction results. To test the efficacy of our method, we conduct experiments on simulated study and Alzheimer’s Disease Neuroimaging Initiative (ADNI) database. The validity and benefit of our model can be shown by the improvement of prediction results and interpretability of visualized procedural bias and lesion features.

Index Terms—Voxel-based Structural Magnetic Resonance Imaging, generalized split linearized bregman iteration, inverse scale space, Alzheimer’s Disease, lesion features, procedural bias, variable splitting

I. INTRODUCTION

ACCURATE prediction of cognitive or disease state is a major goal in neuroimage analysis. One can apply univariate models (e.g. two-sample T-test) to determine which voxels show significant correlations with the task, such as statistical parametric maps (SPMs) [1]. However, the voxel-independence assumption behind such process fails to capture the spatial correlation across different brain regions. Therefore, multivariate approaches in recent years gained more attention in neuroimaging area [2], [3] and proved to be superior

than univariate models in terms of prediction power and interpretability [4], [5], e.g., SVM [2].

In addition to disease prediction, the stable selection of lesion voxels (disease-relevant) is also of concern for neuro-scientists since they can be used to interpret the disease, as a clue for diagnose and further exploration of potential mechanism with therapy [6]. For example, Alzheimer’s Disease (AD), it’s commonly believed that the regions suffer from degenerations are located in parahippocampus gyrus, hippocampus gyrus, temporal lobe, parietal lobe, cingulate gyrus, etc. [6]–[9].

In this paper, we consider using voxel-based analysis, which provides finer scale than Region of interest (ROI)-based method and hence has been increasingly applied [10], [11] with the implementation of structural Magnetic Resonance Imaging (sMRI) that brings no harm to human brains. Due to collection cost, the neuroimage data always suffer from the limited (e.g. dozens of or hundreds of) observations with much higher dimensional feature space (e.g. thousands or millions of features). To avoid over-fitting, existing multivariate machine learning has been applied with regularization function to enforce the pattern among features. Specifically, for neuroimage disease considered in this paper, it is commonly hypothesized that lesion voxels are the most interpretable features to the disease with the following structural sparsity: (i) sparsity: only a subset of features can be regarded as lesion features (ii) geometrically smoothness: each voxel shares the similar extent of degeneration/lesion with its neighbors; (iii) non-negative correlation with the disease: e.g., in Alzheimer’s Disease, the gray matter voxel among patients tends to be atrophied rather than enlarged, compared with that among normal controls.

In the literature, existing models take the task of selection of lesion features and prediction of disease equivalently in terms of optimization. Specifically, one corresponding strategy that often adopted by these machine learning models is that: among the pre-setting grid of regularization parameters that reflects the sparsity levels of selected features, the ones corresponding to the highest prediction result are applied to the model for feature selection. The form of regularization scheme largely depends on the prior knowledge of the underlying structure of the disease-relevant features which may lead to different regularization forms. For instance, lasso [12] assumes sparsity; elastic net [13]

Corresponding author: Lingjing Hu (email: hulj@ccmu.edu.cn), Yuan Yao (email: yuany@ust.hk)

considers additional property of grouping correlated features; group lasso manually define grouping of features [14]–[17] and particularly TV- L_1 (Combination of Total Variation [18], [19] and L_1), takes into account both spatial cohesion and sparsity [18], [20], [21].

However, as pointed out by George Box in [22], "**all models are wrong**", we observe that it's not reasonable to take these two tasks (selection of lesion features, prediction) equivalently in voxel-based neuroimage analysis. One major component of the gap in neuroimage analysis here is dominated by some fixed patterns of biases introduced during the preprocessing of T_1 -weighted image, i.e. the first step of voxel-based neuroimage analysis, such as segmentation and registration of grey matter (GM), white matter (WM) and cerebral spinal fluid (CSF). Such biases are due to scanner difference, different population and especially limitation of spatial normalization, etc. [23]. Part of them can be helpful to the discrimination of subjects from normal controls (NC), but may not be directly related to the disease. For example in sMRI of subjects with Alzheimer's Disease (AD), after spatial normalization during simultaneous registration of GM, WM and CSF, the GM voxels surrounding lateral ventricle and subarachnoid space etc. may be mistakenly enlarged caused by the enlargement of CSF space in those locations [23] compared to the normal template, as shown in Fig. 1. Although these voxels/features are highly correlated with disease, they cannot be regarded as lesion features in an interpretable model, in this paper we refer to them as "Procedural Bias", which should be identified but are neglected in the literature. We observe that it can be explicitly harnessed in our voxel-based image analysis to improve the prediction of disease.

The existence of procedural bias makes the prediction a different goal from selection of lesion features. Existing models fail to take both tasks into consideration. Specifically, as mentioned earlier, models with regularization such as TV- L_1 and n^2 GFL [24], can enforce strong prior of disease in order to capture the lesion features. Although such features are disease-relevant, these models lose some prediction power without consideration of the procedural bias. To pursue a better prediction power, one may utilize the information in procedural bias. For example, the model with ℓ_2 -based regularization (e.g. ridge regression [25], elastic net [13] and graphnet [26]) select strongly correlated features to minimize classification error. However, note that the procedural bias is different from lesion voxels in terms of volumetric information (enlarged v.s. degenerated) and spatial pattern (surrounding distributed v.s. spatial cohesive). Therefore, such regularizations without differentiation of procedural bias from lesion features suffer from poor interpretability and hence may be prone to over-fit. Motivated by the fact that procedural bias is different from pathology-related lesion features, we in this paper propose that the voxels in the whole brain are orthogonally decomposition of three kinds of voxels: (i) atrophied voxels that are contributed to the disease, i.e. lesion features that are interpretable to the disease; (ii) the mistakenly enlarged voxels, i.e. procedural bias which is correlated with the disease however is not belong to the lesion ones; (iii) other voxels that have ignorable correlations with the disease, i.e. null features.

To fulfill the two different tasks that (i) leverage procedural bias into prediction and (ii) stably selection lesion features, we appended the loss function as negative log-likelihood of generalized linear model (GLM) with variable *splitting* term and implement dynamics training in *inverse scale space* induced by *Linearized Bregman* (LB) Distance, namely *Generalized Splitting Linearized Bregman Inverse Scale space* (GSplit LBISS). Specifically, we adopted the variable splitting scheme [27]–[29]: the original parameter space β_{pre} is lifted to a coupled pair $(\beta_{\text{pre}}, \gamma)$ constrained by ℓ_2 regularization: with sparse estimator γ selecting lesion features and dense estimator β_{pre} to additionally capturing procedural bias for better prediction. For training, we proposed a dynamic approach, which generates a family of paired estimators respectively for the above two tasks as solutions in *differential inclusion of inverse scale space*: γ learns the structural sparsity in inverse scale space and β_{pre} that is dense estimator to exploit the procedural bias and lesion features for better prediction. The GSplit LBISS enjoys a simple discretization, namely *Generalized Splitting Linearized Bregman Iteration* (GSplit LBI). At each step, the sparse estimator is returned as the projection of the dense estimator onto the subspace of the support set of γ , satisfies the structural sparsity and hence can be used for selection of lesion features. The remainder of this projection is heavily influenced by the procedural bias, which can be captured by the dense estimator.

Historically, the Linearized Bregman Iteration (LBI) was firstly proposed as sparse recovery optimization algorithm in image denoising [30] and compressed sensing. In [31], [32] firstly consider the LBI as discretization of differential inclusion and presented its statistical property in sparse signal recovery in high-dimensional space. Specifically, under the same condition with Lasso, the LBI can enjoys model selection consistency. In this paper, we generalize it to generalized linear model and structural sparsity, hence the consistent property in feature selection is also inherited. In addition, equipped with variable splitting term that endows the dense parameter some degree of freedom to capture the procedural bias. Therefore, our GSplit LBI can enjoy interpretable feature selection of lesion features and meanwhile the ability of leverage procedural bias to improve prediction power. Besides, our algorithm is easy to implement and is much more efficient than existing sparsity models (e.g. lasso, generalized lasso [33]).

To test the validity, in this paper we apply our model to voxel-based structural MRI (sMRI) analysis for Alzheimer's Disease (AD), which is challenging and attracts increasing attention lately. In detail, equipped with a few reasonable prior knowledge on lesion features of AD, we apply GSplit LBI to the classification of AD, Mild Cognitive Impairment (MCI) and NC. Fitting GSplit LBI on totally 546 samples, with the capture of additional procedural bias, we achieve comparable or better prediction results than state-of-art methods. On the other hand, the selected lesion features are the most stable among all listed models. Moreover, they are stably concentrated in locations such as Hippocampus, ParaHippocampal gyrus and medial temporal lobe, which are believed to be the early damaged regions. Finally, we discuss the differentiation of procedural bias and lesion features by GSplit LBI, future improvements

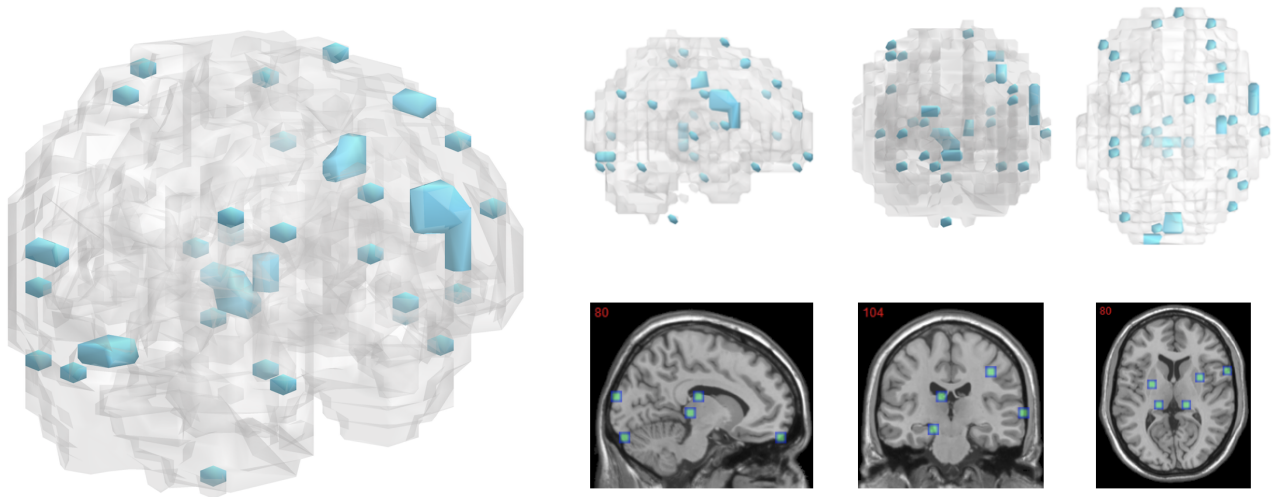


Fig. 1: The top 50 negative voxels of average β_{pre} at the time corresponding to the highest accuracy in the path of GSplit LBI using 8-fold cross-validation. For subjects with AD, they represent enlarged GM voxels surrounding lateral ventricle, subarachnoid space, edge of gyrus, etc.

and extend applications of our methods on finer scales.

This paper is the extended version of the MICCAI'2017 conference report [34] which only gives a brief introduction of GSplit LBI algorithm with preliminary experimental results on cross-validation datasets. In this paper, we extend the report above in both methodology and experiments. In methodology, we give a detailed development of GSplit LBI, as discretization of differential inclusion of inverse scale space, its connection to mirror descent algorithm [35] and computational complexity. In experiments, we conduct additional simulation experiments to illustrate the ability of proposed method to capture both lesion features and procedural bias, and additional classification results of MCI and NC on dataset processed by 3.0T field strength Magnetic Resonance Imaging scanner. Moreover, the results are tested based on held-out datasets, which is a statistically better evaluation of prediction power than merely the cross-validation.

A. Paper Organization

The paper is organized as follows. In Section III, we introduce our loss function for classification and also the structural sparsity priori that the our solution should satisfies. Then we introduce a dual-task differential inclusion of inverse scale space, namely GSplit LBISS and its discretization form called GSplit LBI, including properties variable splitting, regularization solution path and computational complexity; The simulation experiment is introduced and discussed in Section IV, implying that our algorithm can capture both procedural bias and lesion features; Section V conducts experimental results on both disease prediction and lesion features analysis. Besides, we further conduct coarse-to-fine experiment to investigate the locus of selected lesion features. The detailed discussion of experimental results and conclusions are presented in Section VII.

II. RELATED WORK

A. Early Prediction of Neurological Disease

Accurate pre-diagnosis of brain diseases, especially those irreversible ones, is significant for early medical intervention and treatment. Many neurodegenerative diseases can suffer from structural damages for decades before onset of clinical symptoms, which provides a window for early prediction in terms of abnormal brain regions. For example, there could be progressively atrophy in regions such as hippocampus, medial temporal lobe and amygdala, etc. in Alzheimer's Disease (AD) [36]–[38]. To capture these biomarkers for accurate prediction, one can feed into machine learning models preprocessed data on images acquired from Structural Magnetic resonance Imaging (sMRI) (e.g.. T_1 -weighted image), which have been shown to be effective in finding morphological changes [39], as a non-invasive imaging to human brains. For example, one can preprocess sMRI data to extract gray matter (GM) voxels, which suffered loss in volume in diseases such as AD, Frontotemporal dementia [40], Corticobasal degeneration [41], Parkinson's Disease [42]. Together with statistical inference on preprocessed GM voxels for abnormality analysis, i.e., voxel-based morphometry (VBM), it has been shown effective for prediction for AD [43].

However, some biases are inevitably introduced during the procedure of pre-processing steps such as registration, segmentation and modulation, especially in aging patients' brains [44], leading to false-discovery results in VBM. Such biases are mainly due to abnormalities in patients brain, and hence can be regarded as additional signals for classification between normal controls and patients. Again taking AD as an example, as aforementioned, these biases correspond to mistakenly enlarged GM voxels caused by enlarged CSF space in lateral ventricles [45] and subarachnoid spaces, etc. This type of features, which is namely *procedural bias* in this paper, is the first time to be proposed to help prediction. We applied it to AD, which is

irreversible and on the rise recently, and have shown improved prediction accuracy.

B. Feature Selection

In addition to prediction, the interpretability of selected biomarkers/features is another important issue in clinical practice. The feature selection methods can be roughly categorized as two classes: univariate analysis and multivariate analysis. The most typical method in univariate class is two-sample T-test, in which we independently implement hypothesis test voxel-wise, which suffers from high false-discovery-rate (FDR). Other methods, such as BH_q [46], localfdr [47], FDR-HS [48] can alleviate FDR problem, however they treat features independently and hence cannot capture the underlying structure such as spatial cohesion of features.

Multivariate analysis, as an alternative to univariate analysis, is more powerful in utilizing correlations among features and has been successfully utilized in neuroimage analysis. As a sparse feature selection method, the Lasso selects a subset of voxels are correlated with the disease. It ever achieved one of the state-of-the-arts in brain image classification [49], however suffers from low stability of lesion features selection [24]. To overcome this problem, the elastic-net [13] combines the effect of sparsity enforced by lasso-type penalty and strict convexity enforced by ridge-type penalty. In contrast to lasso, it can select clustered area rather than single scattered voxels [50]. To further consider the spatial cohesion of voxels which are embedded in a 3-dimensional space (e.g., atrophied voxels form in cluster such as hippocampus), one can implement Total-Variation (TV)-type sparsity [18] which enforces correlation between voxels and their neighbors. Compared with group lasso penalty which allows predefined groups of voxels to be selected or not simultaneously, the TV can explore new damaged regions rather than pre-defined ones. Particularly, [21] combined lasso-type penalty and TV-type penalty and thus can select atrophied regions. Further, the [24] additionally enforced the positive correlation between the lesion voxels and the disease label, which is reasonable in many neuroimage analysis (such as AD, dementia with Lewy bodies, Parkinson Disease, etc), and achieved more stable result in terms of feature selection and prediction. However, these multivariate analysis suffered from two problems: (i) the multi-collinearity problem [51] which means high correlation among features and hence can select spurious correlations, especially in high-dimensional analysis (ii) failed to consider the aforementioned procedural bias that can improve classification result. In this paper, we proposed to resolve these two problems to achieve better interpretability and prediction power.

III. METHODOLOGY

Problem Setup Our goal is to learn predictor $f : \mathcal{X} \rightarrow \mathcal{Y}$ that classifies the disease label $y \in \mathcal{Y}$ for any $x \in \mathcal{X}$ that collects the neuroimaging data with p voxels. For disease/normal classification, $\mathcal{Y} := \{\pm 1\}$ (+1 denotes the normal control and -1 denotes the disease). To achieve this goal, we are given N training samples $\{\mathbf{x}_i, \mathbf{y}_i\}_1^N$. We denote $\mathbf{X} \in \mathbb{R}^{N \times p}$ and $\mathbf{y} \in \mathbb{R}^p$ as concatenations of $\{\mathbf{x}_i\}_1^N$ and $\{\mathbf{y}_i\}_1^N$. In the

rest, we will consider Alzheimer's Disease as an example to explain our method, whereas with the belief that the whole methodology can also be applied to other neuroimage diseases.

A. Lesion Features and Procedural Bias for Prediction

Generalized Linear Model for Prediction Consider the following discriminative loss for supervised learning:

$$\mathcal{L}_\theta = \mathbb{E}_{(x,y) \sim p(x,y)} - \log p_\theta(y|x), \quad (1)$$

in which $y|x$ is assumed to be generated from *generalized linear model* (GLM):

$$p(\mathbf{y}_i | \mathbf{x}_i, \beta_{\text{pre}}^*, \beta_{\text{pre},0}^*) \propto \exp\left(\frac{\mu_i^* \cdot \mathbf{y}_i - \psi(\mu_i^*)}{d(\sigma)}\right) \quad (2a)$$

$$\mu_i^* = \langle \mathbf{x}_i, \beta_{\text{pre}}^* \rangle + \beta_0^*, \quad \forall i \in \{1, \dots, N\} \quad (2b)$$

where β_{pre}^* (β_0^*) is true (intercept) parameter, $\psi : \mathbb{R} \rightarrow \mathbb{R}$ is link function and $d(\sigma)$ is known parameter related to the variance of distribution, and $\mu_i^* := \langle \mathbf{x}_i, \beta_{\text{pre}}^* \rangle + \beta_0^*$. With Eq. (2), the $\theta := \{\beta_{\text{pre}}, \beta_0\}$ and the negative log-likelihood for sample (x, y) is $\ell(\beta_{\text{pre}}, \beta_0 | x, y) := -\log p_\theta(y|x)$. Given training data $(x_1, y_1), \dots, (x_N, y_N) \stackrel{i.i.d.}{\sim} p(x, y)$, our goal turns to minimize the *empirical risk minimization* (ERM), i.e.,

$$\hat{\mathcal{L}}(\beta_{\text{pre}}, \beta_0) = \frac{1}{N} \sum_{i=1}^N \ell(\beta_{\text{pre}}, \beta_0 | \mathbf{x}_i, \mathbf{y}_i). \quad (3)$$

For our binary classification task, the Eq. (1) degenerates to commonly used logistic regression loss:

$$\hat{\mathcal{L}}(\beta_{\text{pre}}, \beta_0) = \frac{1}{N} \sum_{i=1}^N (\log(1 + \exp(\mu \cdot \mathbf{y})) - \mu \cdot \mathbf{y}). \quad (4)$$

Lesion Features In voxel-based neuroimage analysis, the lesion features have been the main focus since it provides the pathological criterion for the disease. The stable selection of lesion voxels can be helpful for better understanding of the disease, diagnose clinically and drug development. A desired estimator β_{pre} should not only minimize the loss function (Eq 3)), but also satisfy the structural sparsity requirements, which are often enforced by regularization penalty $\Omega(\beta_{\text{pre}})$. In this regard, the loss function turns to

$$\beta_{\text{pre}} = \arg \min_{\beta_{\text{pre}}} \mathcal{L}(\beta_{\text{pre}}, \beta_0) + \Omega(\beta_{\text{pre}}).$$

Such lesion features should satisfy the following *priori* structural sparsities, with details explained in the later:

- 1) $\|\beta_{\text{pre}}\|_1$: ℓ_1 sparsity which implies that only a subset of features are related to the disease.
- 2) $\|D_G \beta_{\text{pre}}\|_1$: Total-Variation (TV) Sparsity, implying that voxel activities should be geometrically clustered or 3D-smooth. The $D_G : \mathbb{R}^V \rightarrow \mathbb{R}^E$ denotes a graph difference operator on $G = (V, E)$ ¹.
- 3) $\mathbb{1}(\beta_{\text{pre}} \geq 0)$: Non-negative Correlation between disease status and volume of voxels.

For 1), it was well known that only a subset of regions are strongly (causally) related to disease status for AD, such as

¹ V is the node set of voxels, E is the edge set of voxel pairs in neighbor on 3-d space, i.e. $D_G \beta_{\text{pre}} = \sum_{(i,j) \in E} (\beta_{\text{pre}}(i) - \beta_{\text{pre}}(j))$

medial temporal lobe and two-side hippocampus [36]–[38]. The [52] has applied Lasso to AD and outperformed SVM. The 2) is due to the spatial coherence of lesion voxels, which means that these lesion features are geometrically clustered into regions such as two-side hippocampus and medial temporal lobe. Enforced by TV-type penalty, the prediction performance can be improved, with corresponding selected lesion features are located into early damaged regions for AD [21]. Further, guided by another prior knowledge that the lesion features are often degenerated for many neuroimage diseases (such as AD, fron-totemporal dementia, corticobasal degeneration, etc.) [24], the 3) can further help improve stability of selection of lesion features and prediction accuracy.

Procedural Bias as a “gap” between prediction and lesion voxels In addition to lesion features, there is another type of features referring some fixed patterns of biases that are correlated with the disease, such as mistakenly enlarged gray matter voxels due to enlargement of neighbouring CSF space, as aforementioned in introduction. These biases are introduced during the procedure of pre-processing step, such as spatial normalization and modulation step in *Voxel-Based Morphometry* (VBM) analysis for Alzheimer’s Disease, hence we name it as *procedural bias*. The procedural bias, which has not been taken into consideration for prediction in the literature, commonly exists as a gap between the selection of lesion features and prediction. In the subsequent section, we are going to introduce our method, namely *Generalized Split Linearized Bregman Iteration* (GSplit LBI), as a dual-task method to handle prediction and stable selection of lesion features simultaneously.

B. Dual-task dynamics via Differential Inclusion of Inverse Scale Space

We introduce two parameters into our model, with the dense parameter for prediction that leverages procedural bias; and the sparse one for selecting lesion features. Such two parameters are enforced via a variable splitting scheme. Specifically, we adopt the variable splitting idea in [27], by introducing an auxiliary variable γ enforced by sparse regularization $J(\gamma)$ to achieve priori structural sparsity requirements of lesion features. Meanwhile we keep it close to $D\beta_{\text{pre}}$ via ℓ_2 regularization: $S_\rho(D\beta_{\text{pre}}, \gamma) := \|D\beta_{\text{pre}} - \gamma\|_2^2$, so as to inherit correlation existed in data between covariates x and label y , supervised by training loss for β_{pre} . Combined with Eq. (3), the updated loss is

$$\hat{\mathcal{L}}(\beta_{\text{pre}}, \beta_0, \gamma) = \hat{\mathcal{L}}(\beta_{\text{pre}}, \beta_0) + \frac{1}{2\nu} \|D\beta_{\text{pre}} - \gamma\|_2^2, \quad (5)$$

where $\nu > 0$ controls the difference between γ and $D\beta_{\text{pre}}$. The $D = [I, \rho D_G^T]^T$ is the concatenation of identity matrix and the Laplacian matrix on graph of voxels embedded in 3d coordinate space. Correspondingly, we can correspondingly view $\gamma = [\gamma_V^T, \gamma_G^T]^T$ as concatenation of γ_V and γ_G . We can then split $\|D\beta_{\text{pre}} - \gamma\|_2^2$ into two terms: $\|D\beta_{\text{pre}} - \gamma\|_2^2 = \|\beta_{\text{pre}} - \gamma_V\|_2^2 + \|\rho D_G \beta_{\text{pre}} - \gamma_G\|_2^2$, which can be explained as the combination of ℓ_1 sparsity and TV sparsity, with $\rho > 0$ controlling the sparsity of lesion voxel and geometrically clustered. In addition, we can enforce $\gamma_V \geq 0$ to incorporate

prior of non-negative correlation between disease label y and lesion voxels. Our goal is thus two folds: (i) we use γ as guidance for selection of lesion features and the structural sparsity of γ can guide β_{pre} to learn corresponding sparsity pattern of lesions on corresponding support set of γ , and (ii) use dense parameters β_{pre} for prediction since it can additionally capture procedural bias located on other positions.

To achieve the structural sparsity of γ and additionally capture procedural bias inherited in the data, we consider the following differential inclusion:

$$\dot{\beta}_0^t = -\nabla_{\beta_0^t} \hat{\mathcal{L}}(\beta_{\text{pre}}^t, \beta_0^t, \gamma^t) \quad (6a)$$

$$\dot{\beta}_{\text{pre}}^t = -\nabla_{\beta_{\text{pre}}^t} \hat{\mathcal{L}}(\beta_{\text{pre}}^t, \beta_0^t, \gamma^t) \quad (6b)$$

$$\dot{v}^t = -\nabla_{\gamma^t} \hat{\mathcal{L}}(\beta_{\text{pre}}^t, \beta_0^t, \gamma^t) \quad (6c)$$

$$v^t \in \partial \mathbf{J}(\gamma^t), \quad (6d)$$

where $v^0 = 0^{p+m}$, $\beta_0^0 = 0$, $\beta_{\text{pre}}^0 = 0^p$, $\gamma^0 = 0^{p+m}$, $\mathbf{J}(\gamma) = \|\gamma\|_1 + \frac{1}{2\kappa} \|\gamma\|_2^2 + \mathbb{1}(\gamma_V \geq 0)$ and $v = \rho + \frac{\gamma}{\kappa} + \lambda$ ($\kappa > 0$) with $[-1, 1] \ni \rho \in \partial \|\gamma\|_1, 0 \geq \lambda \in \partial \mathbb{1}(\gamma_V \geq 0)$. The Eq. (6) generates a regularization solution path from simple to complex, starting from initial points $v^0 = 0$. Specifically, the $v^t = [v_V^{t,T}, v_G^{t,T}]^T$ iterates as gradient descent flow in dual space, until hitting the ℓ_∞ -unit box for v_G^t or hitting 1 for v_V^t , implied by the fact that $v_i^t \in [-1, 1] \leftrightarrow \gamma_i^t = 0$ for $i \in \{|V| + 1, \dots, |V| + |E|\}$; and $v_i^t \geq 1 \leftrightarrow \gamma_i^t = 0$ for $i \in \{1, \dots, |V|\}$. Such a hit makes the corresponding γ_G^t and γ_V^t popping up to non-zero. The earlier the v_G^t (v_V^t) reaches the ℓ_∞ -unit box (or 1), the earlier of corresponding elements in v_G^t (or v_V^t) selected to be non-zeros, which is called the *inverse scale space* property, with "scale" meaning the selection order of elements in γ . When \mathcal{L} denotes the squared loss (corresponds to linear model in Eq. (2a)), $\mathbf{J}(\gamma) = \|\gamma\|_1 + \frac{1}{2\kappa} \|\gamma\|_2^2$, the Eq. (6) degenerates to *Split Linearized Bregman Inverse Scale Space* (Split LBISS), of which the model selection consistency (the support set of γ^t belongs to the true support set when $t \geq t_0$ for some t_0) was established in [27]. In fact, such a statistical analysis in high dimensional space can be traced back to [31] for LBISS with $\nu = 0$ and $D = I$, which is proposed as dynamics form of *Linearized Bregman Iteration* (LBI) that was early known for optimization in compressed sensing and image denoising [30]. The [32] extended such a statistical result to convex loss. The Eq. (6) considers more general structural sparsity that incorporates non-negativity under general linear model (GLM), therefore we called it *Generalized Split Linearized Bregman Inverse Scale Space* (GSplit LBISS).

As a natural extension to generalized linear model and structural sparsity, our GSplit LBISS inherits the statistical property of LBISS. Notably, the GSplit LBISS will fit signals with structural sparsity first, and then tends to over-fit the random noise that induces the distribution of $y|x$ in Eq. (2a). To determine the time t for stopping, we can implement cross-validation, which will be discussed later. At each step in such a regularization solution path, the γ^t can be obtained by back-projection of v^t into primal space with structural sparsity as a priori. Specifically, the Eq. (6d) is equivalent to:

$$\gamma^t = \arg \max_{\gamma} \langle \gamma, v^t \rangle - \mathbf{J}(\gamma), \quad (7)$$

with $\mathbf{J}^*(v^t) := \max_{\gamma} \langle \gamma, v^t \rangle - \mathbf{J}(\gamma)$. We can obtain another β_{les}^t , which is the projection of β_{pre}^t onto the subspace of support set of γ^t , therefore can be regarded the parameters for selecting lesion features. The remainder of such a projection is heavily influenced by procedural bias, which denotes the elements corresponding to large value in such a remainder. The rest with tiny values are regarded as null features/voxels that are not correlated with the disease label, as illustrated by the following orthogonal decomposition of β_{pre} :

$$\beta_{\text{pre}} = \text{lesion Features} \oplus \text{Procedural Bias} \oplus \text{Null Features.} \quad (8)$$

Such a procedural bias can be learned from data in a supervised way, the extent of which is determined by the hyper-parameter ν and t (which will be discussed later). Equipped with ability of selecting lesion features guided by γ^t to select lesion features and additional capture of procedural bias, the β_{pre} can achieve better prediction performance, as will be shown in our experimental section.

Remark III.1. Note that the $\mathbf{J}(\gamma) = \|\gamma\|_1 + \frac{1}{2\kappa} \|\gamma\|_2^2 + \mathbb{1}(\gamma_V \geq 0)$ is differentiable and smooth. Therefore, according to [53, Proposition 3.1], we have $\gamma^t \in \nabla \mathbf{J}^*(v^t)$, replaced Eq. (6d) with which the our GSplit LBISS in Eq. (6) is equivalent to the dynamics form of mirror descent algorithm (MDA) [35], [54]. However, the MDA requires that the penalty function \mathbf{J} is smooth, under which the [53], [54] gave the convergent analysis. With existence of noise, the final point (convergent solution $\lim_{t \rightarrow \infty} (\beta_{\text{pre}}^t, \gamma^t)$ of LBISS with non-smooth \mathbf{J} will over-fit [31]. Therefore, instead of targeting on the convergent result of Eq. (6), we exploits the inverse scale space property to equip GSplit LBISS with early-stopping mechanism, in order to select the solution that satisfies model selection consistency in the whole regularization path. Beyond that, possessed with variable splitting scheme $\frac{1}{2\nu} \|D\beta_{\text{pre}} - \gamma\|_2^2$, at each time-step t the GSplit LBISS will return a dual parameters: the β_{les}^t with structural sparsity and the dense parameter β_{pre}^t that can further capture the procedural bias which is highly correlated with y , endowed with orthogonal decomposition (Eq. (8)).

C. Generalized Split Linearized Bregman Iteration: the simple discretization of GSplit LBISS

The Eq. (6) enjoys a simple discretization, which is called Generalized Split Linearized Bregman Iteration (GSplit LBI) in this paper:

$$\beta_0^{t+1} = \beta_0^t - \alpha \kappa \nabla_{\beta_0^t} \mathcal{L}(\beta_{\text{pre}}^t, \beta_0^t, \gamma^t), \quad (9a)$$

$$\beta_{\text{pre}}^{t+1} = \beta_{\text{pre}}^t - \alpha \kappa \nabla_{\beta_{\text{pre}}^t} \mathcal{L}(\beta_{\text{pre}}^t, \beta_0^t, \gamma^t), \quad (9b)$$

$$v^{t+1} = v^t - \alpha \nabla_{\gamma} \mathcal{L}(\beta_{\text{pre}}^t, \beta_0^t, \gamma^t), \quad (9c)$$

$$\gamma^{t+1} = \kappa \cdot \text{prox}_{\mathbf{J}}(v^{t+1}), \quad (9d)$$

$$S^{t+1} = \text{supp}(\gamma^{t+1}) \quad (9e)$$

$$\beta_{\text{les}}^{t+1} = \mathbf{P}_{S^{t+1}, \geq 0}(\beta_{\text{pre}}^{t+1}), \quad (9f)$$

with $\beta^0 = 0, \beta_{\text{les}}^0 = \beta_{\text{pre}}^0 = 0^p, \gamma^0 = v^0 = 0^{p+m}$, and

$$\text{prox}_{\mathbf{J}}(v) := \arg \min_{\gamma} \frac{1}{2} \|\gamma - v\|_2^2 + \mathbf{J}(\gamma), \quad (10)$$

$$\mathbf{P}_{S, \geq 0}(\beta_{\text{pre}}) = \arg \min_{\substack{D_{S^c} \beta_{\text{les}} = 0 \\ \beta_{\text{les}} \geq 0}} \|\beta_{\text{les}} - \beta_{\text{pre}}\|_2 \quad (11)$$

Algorithm 1 DFS to find connected components for graph $G = (V, E)$

-
- 1: Initialize all vertices as not visited and connected components $\mathcal{C} = \{\}$.
 - 2: $\forall v \in V$,
 - 3: if v is not visited before, define $\mathcal{C}_{\text{new}} = \{v\}$ and call DFSCONNECT($\mathcal{C}_{\text{new}}, v$)
 - 4: else, $\mathcal{C} = \mathcal{C} \cup \mathcal{C}_{\text{new}}$.
 - 5: Output: \mathcal{C} .
-
- 6: _____
- 7: **procedure** DFSCONNECT($\mathcal{C}_{\text{new}}, v$)(a)
- 8: Input: \mathcal{C}_{new}
 - 9: Mark v as visited.
 - 10: $\mathcal{C}_{\text{new}} = \mathcal{C}_{\text{new}} \cup \{v\}$
 - 11: For every $u \in N(v) := \{(u, v) \in E\}$ that is not visited, apply DFSCONNECT($\mathcal{C}_{\text{new}}, v$).
 - 12: **end procedure**
-

with $S := \text{supp}(\gamma)$ and it returns the parameter β_{les} for selecting lesion features. With Eq (10), the Eq. (9d) is equivalent to $\gamma_V = \kappa \cdot \max(z_V - 1, 0)$ and $\gamma_G = \kappa \cdot \text{sign}(z_G) \cdot \max(|z_G| - 1, 0)$. For Eq. (10), since $\text{supp}(\gamma) = \text{supp}(\gamma_V) \cup \text{supp}(\gamma_G)$ and $\text{supp}(\gamma_G) \subseteq E$ defines an edge set on node $V := \{1, \dots, p\}$, we can find the set of connected components \mathcal{C} of $\tilde{G} = (V, \text{supp}(\gamma_G))$ via *Depth-First Search* (DFS) algorithm as introduced in algorithm 1 with computational complexity $\mathcal{O}(p + m)$. The elements belonging to the same connected component share the same value in terms of β_{les} . Suppose there are T connected components for $\tilde{G} = (V, \text{supp}(\gamma_G))$, i.e., $\mathcal{C} = \{i_1, \dots, i_{n_t}\}_{t=1}^T$, then for all $t \in \{1, \dots, T\}$ we have

$$\beta_{\text{les}}(i_t) = \begin{cases} 0, & \forall i_t \in \text{supp}(\gamma_V) \\ \max\left(\frac{1}{n_t} \sum_{k=1}^{k=n_t} \beta_{\text{pre}}(i_k), 0\right), & \forall i_t \in \text{supp}(\gamma_V)^c \end{cases} \quad (12)$$

Setting hyper-parameters (i) The $t^k = k \cdot \alpha$ is regularization hyper-parameter, which is often chosen by cross validation [55]. Parameter ρ is a tradeoff between geometric clustering and voxel sparsity. Heuristically, Its choice depends on the quality of data, e.g. for data with lower resolution of MRI images, comparably larger ρ is suggested since in this case more clustered features will be selected to suppress the noise. (ii) The κ is a damping factor which can be used to reduce bias with a large value. Specifically, it's shown in [55] that as κ becomes larger, the solution path of LBI looks similar to that of Bregman ISS (Inverse Scale Space), which returns a solution path with bias-free estimators. However, too large κ results in more variance and also lower the convergence speed. (iii) The α in LBI for discretization is step size, which is the tradeoffs between statistical and computational issues [56]. One can generate a 'coarse' regularization path with larger value of α though, it fails to satisfy statistical properties, such as recovering true signal set. On the other hand, smaller α makes the solution path 'denser', hence lower the computational speed. To ensure the stability of iterations, one may choose $\alpha < \nu / \kappa (1 + \nu \Lambda_H + \Lambda_D^2)$ [57] with Λ_A denoted as the largest singular value of general matrix A and H here denotes Hessian

matrix of $\mathcal{L}(\beta_0, \beta_{\text{pre}})$ (iv) The choice of ν is task-dependent, as shown in Fig. 2. For lesion feature analysis, β_{les} with a small value of ν is helpful to enhance stability of feature selection. Note that when $\nu \rightarrow 0$, $\|\beta_{\text{pre}} - \beta_{\text{les}}\|_2 \rightarrow 0$ in the whole path. In this case β_{les} will select lesion features with a good fitness of data. For prediction of disease, β_{pre} with appropriately larger value of ν has more degree of freedom to leverage procedural bias into prediction. We will discuss it for details later.

Exploitation of Procedural Bias The capture of procedural bias is affected by hyper-parameter ν and t . With larger value of ν , the β_{pre} has more degree of freedom to capture procedural bias, as illustrated in Fig. 3. With smaller value of ν , the parameter space of $(\beta_{\text{pre}}, \gamma)$ is located into a lower dimensional space, which may result in β_{les} with more stability, as illustrated in Fig. 2.

As t grows, the $\beta_{\text{les}}(t)$ is with less sparse regularization effect, hence converges to β_{pre} , i.e., $\|\beta_{\text{pre}}(t) - \beta_{\text{les}}(t)\|_2 \rightarrow 0$, as illustrated in Fig. 4. In this case (i.e. t is large), $\beta_{\text{les}}(t)$ may overfit to the noise, hence can select redundant features, which will also deteriorate the performance of β_{pre} . Hence, an early stopping strategy is necessary to implement to avoid overfitting, as mentioned earlier.

Computational complexity For ℓ_1 -minimization, for each regularization hyper-parameter λ , a popular iterative algorithm to solve the minimization problem is the well-known iterative soft-thresholding algorithm (ISTA) ([58] and references therein). To tune λ , one needs to run ISTA until convergence for each λ , which is time-consuming. In a contrast, LBI returns the full regularization path where estimators in each iteration is function of sparsity level [55], [59] regularized by t_k . The model selection consistency of such a regularization path has been theoretically discussed in [55] for the square loss and in [60] for general losses (including the logistic regression). More importantly, at each t_k the minimizer of sub-problem and the β_{les} can be written in a closed form achieved by soft-thresholding operator and DFS algorithm. In this respect, LBI only runs a single path with early stopping time t^* determined via cross-validation. In addition, by taking step size α small enough and κ large enough to ensure the stability of iterations, one can achieve sign-consistency and minimax optimal ℓ_2 -error bounds [55] under the same conditions as ℓ_1 -regularization (Lasso) but with less bias [31]; while ℓ_1 -minimization deteriorates true signals due to its bias. For each iteration, the time complexity of LBI and ISTA with logistic regression loss is $O(np)$; LBI returns the full regularization path at $O(npk)$ where k is the number of iterations, while with $O(npk)$ iterations ISTA only returns a single estimate at particular λ . For GSplit LBI, with cost at computation for gradient of variable splitting term, the time complexity is $O(npk + mpk)$. Although with additional $O(mp k)$, it can cost much less than ℓ_1 -minimization which costs $O(n_\lambda npk)$, where n_λ is the number of λ in the grid of regularization parameters. However, it should be noted that for GSplit LBI, the number of iterations, k is determined by α , κ and ν .

A simulation experiment is conducted to compare computational efficiency of GSplit LBI and ℓ_1 -minimization, in terms of $\text{card}(\beta_{\text{les}}) := |\text{supp}(\beta_{\text{les}})|$ and $\ell(\beta_{\text{pre}}^k)$. For experimental setting, we set $n = 100$ and $p = 80$, $D = I$ and $X \in \mathbb{R}^{n \times p}$ and

$X_{i,j} \sim N(0, 1)$. $\beta_i^* = 2$ for $1 \leq i \leq 4$, $\beta_i^* = -2$ for $5 \leq i \leq 8$ and 0 otherwise, y is generated via logit model given X and β^* . For GSplit LBI, we run a single path and compute $\text{card}(\beta_{\text{les}}^k)$ and $\ell(\beta_{\text{pre}}^k)$ at each iteration. For ℓ_1 -minimization, we set a sequence of λ and run FISTA [58], an accelerate version of ISTA for every λ . Besides, we employ the computation strategy, i.e. take the solution of λ_k as the initial solution for the next λ_{k+1} . For each λ , the algorithm stops as long as either of following stopping criteria is satisfied:

$$\|\beta^{k+1} - \beta^k\|_1/p < 10^{-8}, \quad \|\nabla \ell(\beta^k)\|_\infty < 10^{-6}$$

All experiments were implemented in MATLAB R2014a 64-bit on a MacBook Pro laptop with Mac OSX 10.12.4, 2.6 GHz Intel Core i5 and 8 GB 1600 MHz DDR3 memory. Fig. 5 shows the function curve of cardinality of solution support and loss versus the accumulated computational time and number of iterations. As shown, the GSplit LBI is convergent faster than FISTA in terms of cardinality of support and loss function.

IV. SIMULATION

In this experiment, we conduct a simulation experiment to illustrate the effect of selecting both lesion features and procedural bias for GSplit LBI. To simulate voxel-based neuroimage scenario, the lesion features are set to be sparse, positively correlated with disease label and clustered into a region (Red Center in "original" figure in Fig. 6); while the ground truth of procedural bias (Blue Corner in "original" figure in Fig. 6) is less clustered and negatively correlated with disease label. We show in the following that (1) β_{les} capture lesion features (2) β_{pre} capture both kinds of features.

In details, we set $N = 400$. The feature space is a 2-d squared images with $p = 9 \times 9 = 81$ pixels. We denote \cdot . For the true signal vector $\beta^* \in \mathbb{R}^{9 \times 9}$, the center with size 5×5 representing lesion features are assigned with value 3; while the four corner pixels representing procedural bias are with value -3; other pixels are assigned with value 0. $X \in \mathbb{R}^{N \times p}$ denotes N i.i.d samples with each generated from $N(0, I_p)$, i.e.,

$$P(y_i = \pm 1) = \frac{\exp(\langle x_i, \beta^* \rangle \cdot y_i)}{1 + \exp(\langle x_i, \beta^* \rangle \cdot y_i)}$$

where x_i denotes the i th row/sample of X . For GSplit LBI, we set $\kappa = 80$, $\nu = 2$ and $\alpha = \nu/\kappa(1 + \nu\Lambda_X^2 + \nu\Lambda_D^2)$.

After getting β_{les}^t and β_{pre}^t for some t , the positive and negative coefficients can be projected to **Red** and **Blue** color, respectively. In more details, for positive features, their **Red** channel value is normalized by dividing the greatest value. Besides, the **Green** and **Blue** channels value of positive features are all kept to 0. The procedure is similar to the projection of the negative features into **Blue** color. After projection, It can be shown from Fig. 6 that β_{les} can successfully recover lesion features (Red Center), the β_{pre} can successfully recover both lesion features and procedural bias (Blue Corner).

V. APPLICATION TO ADNI DATASET

In this section, we apply our method on real-world data of Alzheimer's Disease.

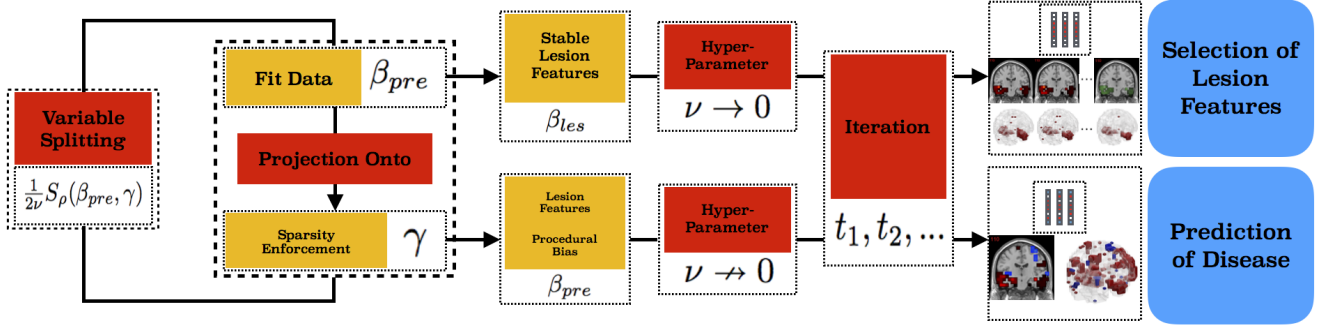


Fig. 2: Illustration of how *GSplit LBI* works. The gap between β_{pre} for fitting data and γ for sparsity is controlled by $S_\nu(\beta_{pre}, \gamma)$. The estimate β_{les} , as a projection of β_{pre} on support set of γ , can be used for stable lesion feature analysis when $\nu \rightarrow 0$ (Section VI-B). When $\nu \rightarrow 0$ (Section VI-A) with appropriately large value, β_{pre} can be used for prediction by capturing both lesion features and procedural bias.

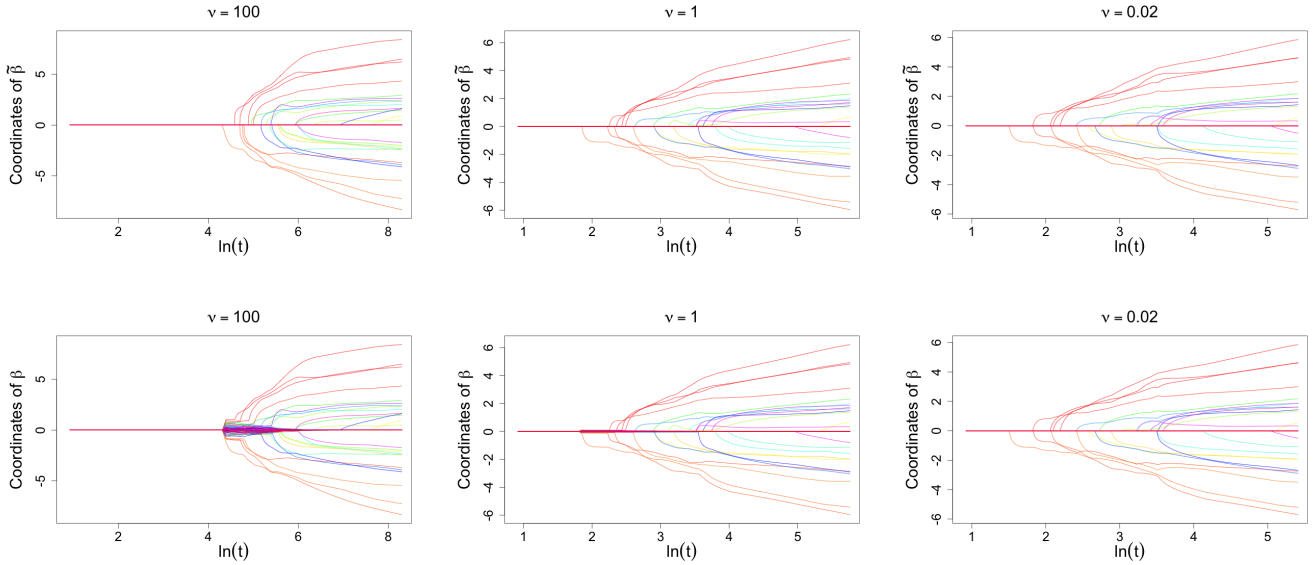


Fig. 3: Comparison of regularized solution path between β_{pre} (denoted as β in the figure) and β_{les} (denoted as $\tilde{\beta}$ in this figure) when $\nu = 100, 1, 0.02$. Each color represents the solution path for each variable. As shown the paths of β_{pre} and β_{les} look more similar with each other as ν decreases.

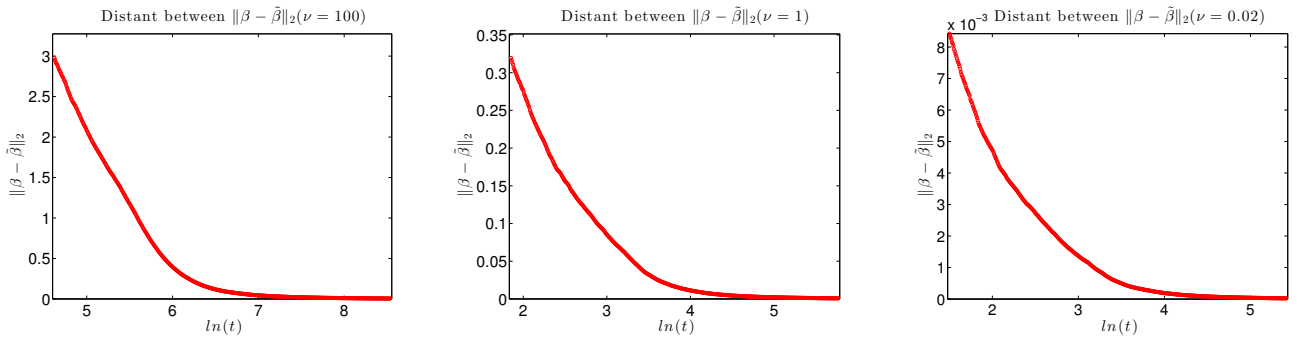


Fig. 4: $\|\beta_{pre} - \beta_{les}\|_2$ in the regularized solution path when $\nu = 100, 1, 0.02$. As ν decreases, the distance of $\beta_{pre}(t)$ and $\beta_{les}(t)$ are tended to be with smaller distance. Her " β " denotes β_{pre} and " $\tilde{\beta}$ " denotes β_{les} .

A. Acquisition of data

The data are obtained from Alzheimer's Disease Neuroimaging Initiative (ADNI) <http://www.loni.ucla.edu/ADNI>

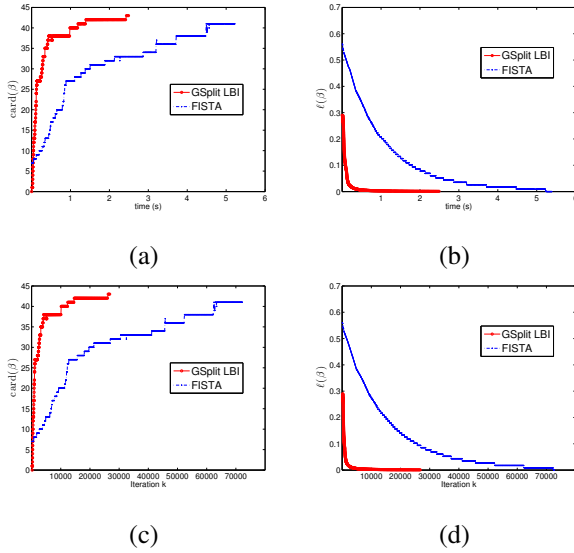


Fig. 5: (a)&(b) show the function curve of support cardinality and loss versus computational time. (c)&(d) show the them versus number of iterations.

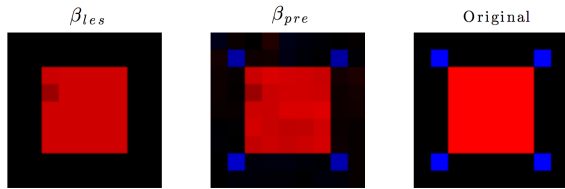


Fig. 6: Simulation results. The lesion features(red) can be recovered by both β_{les} and β_{pre} ; the procedural bias(blue) can be recovered by β_{pre}

database. Starting from October 2004, ADNI is a long-period non-profit project that was originally funded by National Institute on Aging (NIA), National Institute of Bioimaging and Bioengineering (NIBIB), National Institutes of Health (NIH), pharmaceutical Industry and other private foundations. ADNI GO was launched in 2010 to continue the study of ADNI and started to focus on participants who exhibit the very beginning stages of memory loss. In 2011, ADNI 2 was launched as the third phase of ADNI study. One of the major goal is to efficiently predict mild cognitive impairment (MCI) and early Alzheimer’s disease(AD) in clinical practice [61].

The ADNI contains various types of data, including images from sMRI, PET and CSF biomarkers. In this paper, we implement analysis on sMRI, which shows high rates of brain atrophy for AD and hence has high statistical power for determining treatment effects [61]. The data are acquired from 1.5T and 3.0T (namely 15 and 30) field strength Magnetic Resonance Imaging scanners. Specifically, the 15 dataset contains 64 AD patients, 90 NC and 110 MCI patients; while 30 dataset contains 66 AD patients, 110 NC and 106 MCI.

The overall subject information is listed in table I and II. ²

TABLE I: The Demographic data for subjects from 1.5T MRI scan. MMSE=Mini-Mental State Examination

1.5T	AD	MCI	NC
Size	64	110	90
Gender (M/F)	43/21	77/33	61/29
Age (mean \pm SD)	74.55 \pm 7.22	73.93 \pm 7.56	75.07 \pm 4.46
Education (mean \pm SD)	14.72 \pm 3.11	16.30 \pm 2.84	16.49 \pm 2.59
Hand (R/L)	61/3	99/11	83/7
MMSE	23.45 \pm 2.00	27.28 \pm 1.838	28.96 \pm 1.04

TABLE II: The Demographic data for subjects from 3.0T MRI scan. MMSE=Mini-Mental State Examination

3.0T	AD	MCI	NC
Size	66	106	110
Gender (M/F)	43/23	67/39	54/56
Age (mean \pm SD)	74.38 \pm 9.32	72.25 \pm 7.50	73.07 \pm 5.92
Education (mean \pm SD)	15.59 \pm 3.01	16.36 \pm 2.56	16.65 \pm 2.58
Hand (R/L)	60/6	98/8	99/11
MMSE	23.11 \pm 2.05	27.41 \pm 1.74	28.93 \pm 1.26

B. Image Preprocessing

The image preprocessing follows the DARTEL (Diffeomorphic Anatomical Registration Through Exponentiated Lie Algebra) Voxel-based morphometry (VBM) pipeline [43]. VBM is the commonly adopted method to study the of local differences of gray matter concentration among population of subjects. During this process, the preprocessing of registration is necessary, for which the DARTEL is implemented. In the spatial normalization step during registration, the brain templates based on anatomical images of subject groups are made and normalized onto the standard Montreal Neurological Institute template, which makes DARTEL be able to achieve more accurate inter-subject registration of brain images. After implementing this preprocessing step, the final input features consist of 2,527 $8 \times 8 \times 8mm^3$ size voxels with average values in GM population template greater than 0.1. Experiments are then designed on four tasks, 1.5T AD/NC, 3.0T AD/NC, 1.5T MCI/NC and 3.0T MCI/NC (namely, 15ADNC, 30ADNC, 15MCINC and 30MCINC, respectively).

C. Validation

To evaluate the performance of our model, we used a train-test split strategy to compute the classification accuracy (acc), sensitivity (sen) and specificity (spe), which are defined as

$$acc = \frac{\#\{i|\hat{y}_i = y_i\}}{N}$$

$$sen = \frac{\#\{i|\hat{y}_i = y_i = -1\}}{\#\{i|y_i = -1\}}$$

$$spe = \frac{\#\{i|\hat{y}_i = y_i = 1\}}{\#\{i|y_i = 1\}}$$

where \hat{y} is the predicted outcome (-1 denotes AD). In more details, we split datasets into 70% training datasets and 30% test

²For subject IDs, please refer to data statement <https://github.com/swxw/xiaoxiao/ADNI/blob/master/GSplit%20LBI%20SID.pdf>.

datasets. Under exactly the same experimental setup, comparisons are made between GSplit LBI and other classifiers: SVM, MLDA(univariate model via t-test + LDA) [62], Graphnet [26], lasso [12], Elastic Net, TV+L₁ and n²GFL. The optimal hyper-parameters of each model are determined via 8-fold cross-validation on training set. Then β_{pre} for prediction on test set is learned on the whole training set implemented with the optimal parameters. To reduce random partition bias, we repeated this procedure for 10 times. For GSplit LBI, the κ and ν are set to 10 and 0.2, respectively; α = ν/κ(1 + νΛ_X² + Λ_D²)³. For GSplit LBI, ρ is chosen from {0.5, 1, ..., 5}, The regularization coefficient λ is ranged in {0, 0.05, 0.1, ..., 0.95, 1, 2, 5, 10} for lasso and 2^{-20, -19, ..., 0, ..., 20} for SVM. For other models, parameters are optimized from λ : {0.05, 0.1, ..., 1, 2, 5, 10} and ρ : {0.5, 1, ..., 5} (in addition, the mixture parameter α : {0, 0.05, ..., 0.95} for Elastic Net).

VI. RESULTS AND ANALYSIS

We firstly compare GSplit LBI with other models according performance on 8-fold cross-validation in training set. It's noted that although K-fold cross-validation may underestimate the prediction error, it can measure the optimistic performance of one's model that it can achieve. As shown from table III that, the results of our model are better or comparable than other models on all tasks. Further, to accurately access the prediction power of GSplit LBI and other models, the results on 30% held-out test sets is reported. Such held-out test sets can measure the generalization to new data, hence the performance on those sets provide the true classification error. To reduce bias of randomness, the process is implemented for 10 times and the mean values are reported. It's shown in table IV that GSplit LBI also yields better or comparable out-of-sample classification error than other models, with accuracies of 86.31%, 88.08%, 62.67% and 65.94% on 15ADNC, 30ADNC, 15MCINC and 30MCINC, respectively. Note that Graphnet can yield better results than TV + l₁ and n²GFL since it relaxes the piece-wise constant enforcement. However, it can select more redundant features than necessary, which will be discussed later.

A. Procedural Bias Captured by β_{pre}

Recall that positive (negative) features represent degenerate (enlarged) voxels. By projecting β_{pre} onto the subspace of γ (Eq. (10)), β_{les} can be returned at each iteration. Note that with non-negative constraint, the β_{les} only select lesion features while β_{pre} has the capability of selecting other negative features to fit data better. To see such an effect of β_{pre} in comparison with β_{les}, we plot accuracy curve on validation sets v.s. time t due to the path property of our algorithm. The result of 30ADNC is used as an illustration. It can be seen in Fig. 7 that (1) accuracy of β_{pre} is higher than β_{les} in the whole path; (2) before reaching its highest accuracy, i.e. t₆, β_{pre} shares the similar trend of accuracy with β_{les}; after t₆, they gradually converge to each other when the GSplit LBISS starts to over-fit. To explain (2), we compare the positive (lesion) features selected by β_{pre} and β_{les} in six points during the regularization

TABLE III: Comparisons of GSplit LBI with other models(cross-validation)

	15ADNC			30ADNC		
	ACC	SEN	SPE	ACC	SEN	SPE
MLDA	84.54%	83.33%	85.40%	87.50%	90.21%	85.84%
SVM	81.94%	59.11%	93.69%	86.94%	74.93%	95.24%
Lasso	82.69%	74.22%	88.73%	85.00%	72.98%	92.34%
Elastic Net	83.52%	71.78%	91.90%	88.95%	77.02%	96.23%
Graphnet	85.09%	76.00%	91.27%	87.26%	73.19%	95.84%
TV + l ₁	83.16%	74.89%	88.73%	85.73%	74.89%	92.34%
n ² GFL	83.70%	74.89%	90.00%	84.84%	69.58%	94.16%
Ours(β _{pre})	87.22%	81.33%	91.43%	89.11%	81.49%	93.77%
	15MCINC			30MCINC		
	ACC	SEN	SPE	ACC	SEN	SPE
MLDA	66.19%	63.16%	69.89%	67.04%	65.33%	68.70%
SVM	70.29%	74.54%	63.81%	65.13%	51.82%	78.05%
Lasso	63.93%	70.78%	55.56%	65.07%	60.67%	69.35%
Elastic Net	72.86%	78.70%	65.71%	70.20%	66.13%	74.16%
Graphnet	72.50%	78.05%	65.71%	69.34%	60.53%	77.92%
TV + l ₁	68.36%	72.73%	63.02%	66.18%	62.67%	69.61%
n ² GFL	69.14%	76.62%	60.00%	68.23%	64.00%	72.34%
Ours(β _{pre})	72.93%	78.31%	66.35%	70.72%	68.67%	72.65%

TABLE IV: Comparisons of GSplit LBI with other models on test dataset

	15ADNC			30ADNC		
	ACC	SEN	SPE	ACC	SEN	SPE
MLDA	84.35%	81.05%	86.67%	86.92%	90.53%	84.85%
SVM	83.49%	68.42%	94.07%	85.00%	68.42%	94.55%
Lasso	86.31%	77.89%	92.22%	82.12%	66.32%	91.21%
Elastic Net	86.31%	76.32%	93.33%	86.15%	72.11%	94.24%
Graphnet	84.57%	74.21%	91.85%	86.92%	71.58%	95.76%
TV + l ₁	79.35%	68.95%	86.67%	84.04%	68.42%	93.03%
n ² GFL	83.70%	71.58%	92.59%	83.46%	67.89%	92.42%
Ours(β _{pre})	86.31%	78.95%	91.48%	88.08%	76.84%	94.55%
	15MCINC			30MCINC		
	ACC	SEN	SPE	ACC	SEN	SPE
MLDA	58.17%	53.03%	64.44%	62.34%	58.39%	66.06%
SVM	61.00%	64.24%	57.04%	65.31%	54.19%	75.76%
Lasso	53.83%	60.00%	46.30%	64.06%	59.68%	68.18%
Elastic Net	59.83%	64.85%	53.70%	65.78%	61.61%	69.70%
Graphnet	61.13%	64.85%	56.67%	66.09%	57.42%	74.24%
TV + l ₁	54.33%	60.71%	46.67%	61.56%	53.55%	69.09%
n ² GFL	60.50%	66.97%	52.59%	63.13%	61.61%	64.55%
Ours(β _{pre})	62.67%	68.18%	55.93%	67.03%	67.10%	66.97%

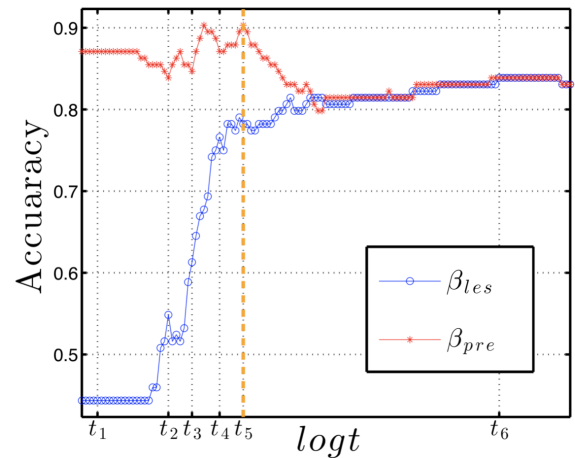


Fig. 7: Accuracy curve of β_{pre} and β_{les}. Red curve represents β_{pre}, blue curve represents β_{les}.

³For logit model, α < ν/κ(1 + νΛ_H² + νΛ_X²) since Λ_X > Λ_H.

solution path. The 3-d images and 2-d slice images are also shown. The brighter of the color of the voxel, the larger of the value of it. We can see from Fig. 8 that β_{les} is more similar with β_{pre} as t progresses. From the start (at t_1), almost all features are nonzeros and assigned with comparably large values for β_{pre} while no features selected for β_{les} . As β_{les} continuously selects features located near 2-side hippocampus and thalamus on t_2, t_3, t_4 , the corresponding features are brighter/larger than others in β_{pre} and the image looks more similar to β_{les} . At t_5 , β_{pre} captures features located in those atrophied areas from β_{les} and achieves the highest accuracy in the whole path. After t_5 , the β_{les} starts to fit noise other than lesion features since with less regularization effect, leading to convergence of β_{les} to β_{pre} .

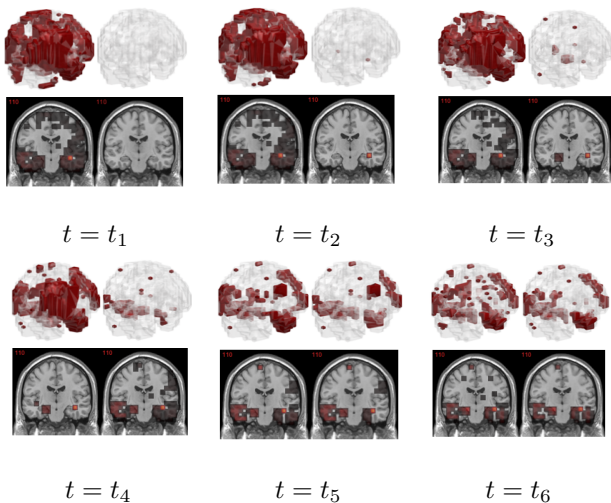


Fig. 8: The 2-d 110 brain slices of β_{les} and β_{pre} at six time points above.

To explain (1), note that in addition to similar lesion features of β_{pre} and β_{les} , β_{pre} can also capture additional procedural bias on other regions to achieve better fitness of data. Specifically, at β_{pre} 's highest accuracy (t_5), the top 50 negative (enlargement) voxels of average β_{pre} are recorded, as shown in Fig. 1. We can see that most selected voxels are located in GM voxels near lateral ventricle or subarachnoid space etc., which are different from locations of lesion ones.

B. Gray Matter lesion feature analysis

It's shown in Fig. 2 that by introducing variable splitting term, the tasks of prediction and selecting lesion features can be incorporated and solved by two different estimators. Hence, in addition to prediction power, the lesion feature analysis is another important component for evaluating our model. One of the main concern in such task is whether the selected lesion features are stable, which is important in terms of trustworthy to regard the lesion features as indicators in clinical diagnosis. To quantitatively evaluate such a stability, multi-set Dice Coefficient (mDC) is applied as a measurement and defined as:

$$mDC := \frac{10|\cap_{k=1}^K S(k)|}{\sum_{k=1}^K |S(k)|}$$

where K is the number of folds in cross-validation and $S(k)$ denotes the support set of solution vector in k -th fold [24], [63]. We compute mDC for β_{les}^k at t_k corresponding to the highest accuracy of β_{les} via 10-fold cross-validation on the whole dataset. The 30ADNC task is again applied as an example. As shown from Table V, when $\nu = 0.0004$ (corresponding to $\nu \rightarrow 0$ in Fig. 2), the β_{les} of our model can obtain more stable lesion feature selection results than other models with comparable prediction power. Besides, the average number of selected features (line 3 in Table V) are also recorded. Note from Table V and Fig. 9 that although elastic net and graphnet (with ℓ_2 regularization) are of slightly higher accuracy than β_{les} , they select much more features than necessary.

In Fig. 10, the overlapped features across all 10 folds of different models are illustrated (corresponding to their highest accuracy for cross-validation). We can see that, the features selected by lasso are too scattered to clustered into regions. Although the elastic net can select more correlated features, they do not form into cluster with no prior of 3D smooth. The features selected by graphnet are redundant (with an average of 1,969.2, among all 2,527 features), although they can form into regions. For n^2 GFL and GSplitted LBI, they consider non-negative, sparsity and 3D smooth sparsity requirements. As shown, the selected features are located in hippocampus, parahippocampal gyrus and medial temporal lobe etc., which are believed to be early damaged regions for AD patients. On the contrary, the other three models can select voxels that are located in other regions, which may be hard to explain the disease.

C. Tuning parameters

In our algorithm, parameter ν balances the prediction task and stability of feature selection, i.e. when $\nu \rightarrow 0$, the β_{les} can select features with better fitness of data and more stability; when ν gets larger, the β_{pre} will be assigned with more capability to select procedural bias. Therefore, the choice of ν is task-dependent. In this experiment, ν is set to 0.2 for prediction of disease and 0.0004 for lesion feature analysis.

The regularization parameter t and parameter ρ are determined via cross-validation. For t , we can see that on one hand β_{pre} will be constrained by β_{les} to continuously select more lesion features as t progresses; on the other hand, there will be less capability of β_{pre} to capture procedural bias during the path since the regularization effect of β_{les} decreases as t grows. At the optimal point, β_{pre} can appropriately "learn" lesion features from β_{les} and is not equal to β_{les} since it's also assigned with enough capability to utilize procedural bias to further improve prediction result compared to β_{les} . When β_{pre} and β_{les} converge together, some redundant features can be selected by β_{les} ; besides, β_{pre} will lose the capability to capture procedural bias, in which case the accuracy will decrease.

Parameter ρ can be treated as trade-off between geometric clustering and voxel sparsity, i.e. for larger value of ρ , the model tends to select more clustered features; for smaller value of ρ , features are tended to more scattered. Heuristically, the choice of ρ depends on the quality of data, e.g. for data with lower resolution of MRI images, comparably larger ρ is suggested since in this case more clustered features will be

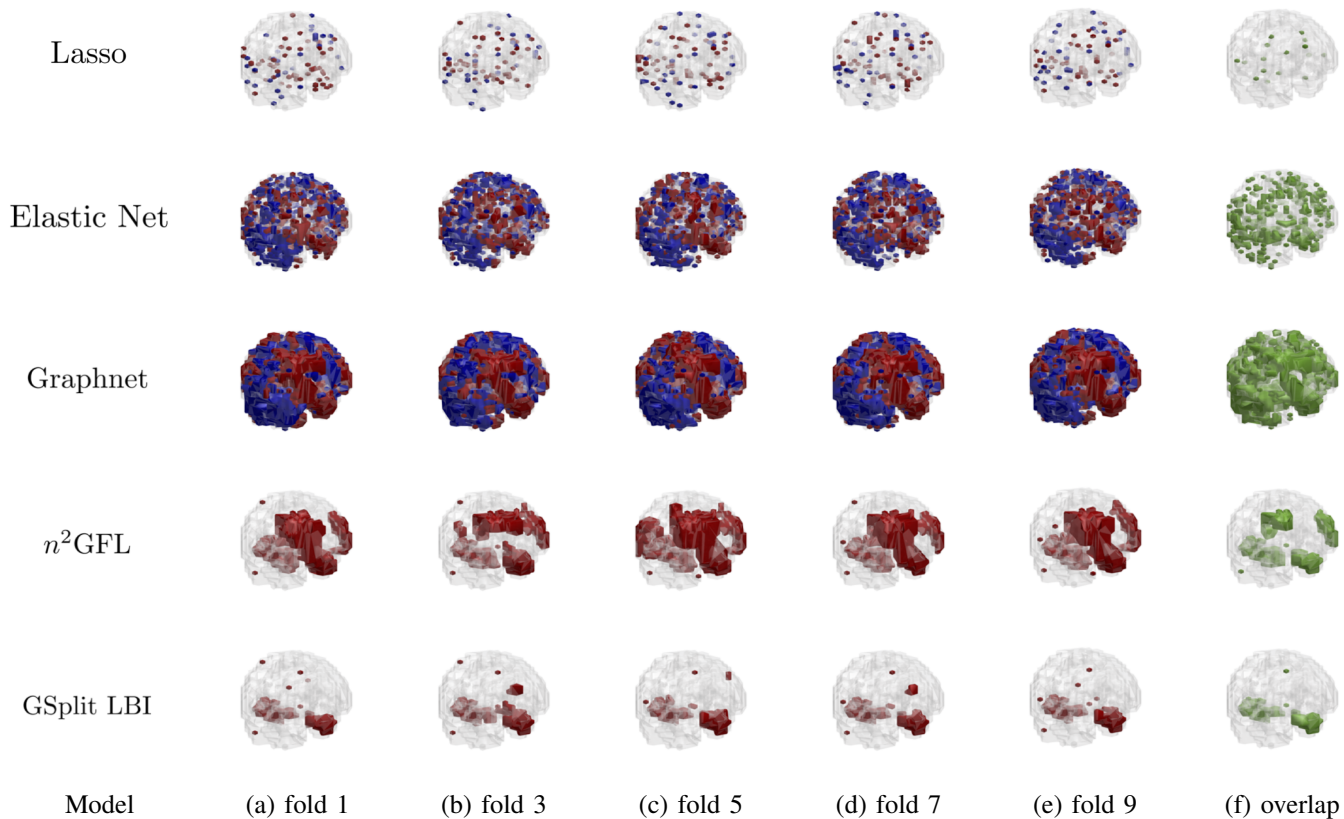


Fig. 9: Selected lesion features across different folds by different models shown in 3-d brain images. The 1-5th row illustrated lasso, elastic net, graphnet, n^2GFL and β_{les} of GSplit LBI, respectively. (a)-(e): Results of fold 1,3,5,7,9. (f): The overlapped features in all 10 folds.

TABLE V: mDC comparisons between GSplit LBI and other models

	Lasso	Elastic Net	Graphnet	n^2GFL	GSplit LBI(β_{les})
Accuracy	87.50%	89.77%	90.34%	87.50%	89.20%
mDC	0.1973	0.4524	0.6216	0.5362	0.7628
$\sum_{k=1}^{10} S(k) /10$	81.1	963.7	1,969.2	443.9	131.1

selected to suppress the noise. Take our experiments as an example, for tasks of 15ADNC and 15MCINC, the ρ selected by cross-validation are 1.95 and 2.35, respectively; for tasks of 30ADNC and 30MCINC, the ρ selected by cross-validation are 1.35 and 1.65, respectively. Such results agree with the common sense since normally 3.0T MRI scanner can produce images with higher resolution than 1.5T MRI scans.

D. Coarse-to-fine experiments

To further investigate the locus of lesion features, an experiment with coarse-to-fine is conducted. Specifically, we project the overlapped voxels with $8 \times 8 \times 8 mm^3$ size (shown in Fig. 10 (e)) onto MRI images with more finer scale voxels, i.e. $2 \times 2 \times 2 mm^3$ size. Totally 4,179 voxels are served as input features after projection. Again, the GSplit LBI is implemented using 10-fold cross validation. The accuracy on validation set of β_{les} is 90.34% and on average 634.0 voxels are selected and they belong to parts of lesion regions, such as those located in

Hippocampal Head, Medial Temporal Lobe, as shown in (d) of Fig. 11.

VII. CONCLUSIONS

In this paper, a novel iterative variable splitting algorithm, based on differential inclusion of inverse scale space, is proposed to stably select lesion features and leverage procedural bias into prediction in neuroimage analysis. With a variable splitting term, the estimators for prediction and selecting lesion features can be separately pursued and mutually monitored under a gap control. The gap here is dominated by the procedural bias, some specific features crucial for prediction yet ignored in a priori disease knowledge. With experimental studies conducted on 15ADNC, 30ADNC, 15MCINC and 30MCINC tasks, we showed that: (1) the leverage of procedural bias can lead to significant improvements in both prediction and model interpretability, (2) the selected lesion features are with high stability and are located in regions that are believed to be early damaged. We

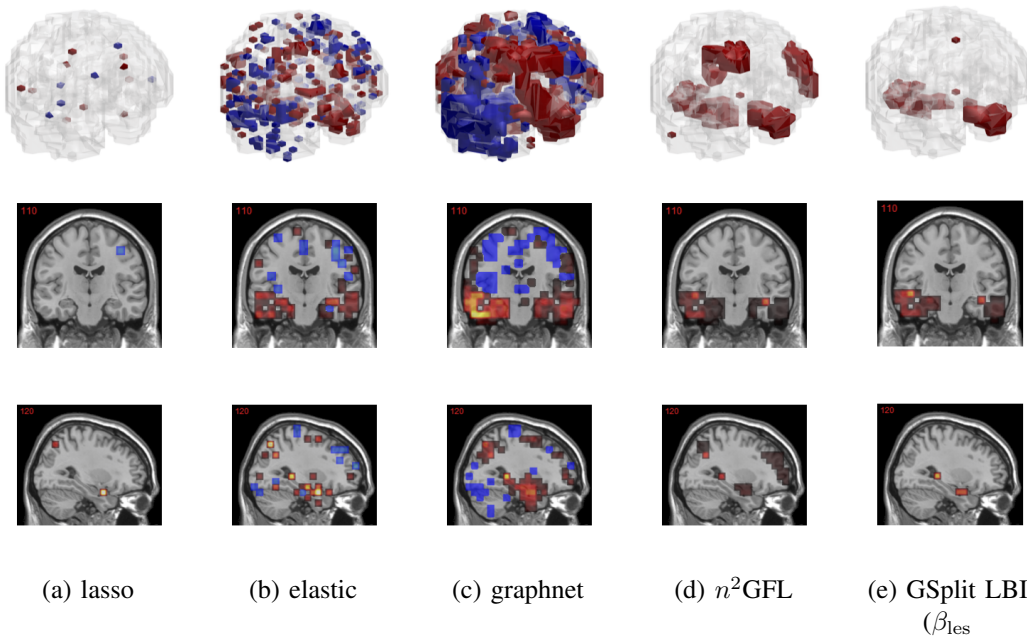


Fig. 10: Overlapped features of different models shown in 2-d 110 brain slices. Red represents lesion features; blue represents procedural bias.

REFERENCES

- [1] K. J. Friston, A. P. Holmes, K. J. Worsley, J.-P. Poline, C. D. Frith, and R. S. Frackowiak, "Statistical parametric maps in functional imaging: a general linear approach," *Human brain mapping*, vol. 2, no. 4, pp. 189–210, 1994.
- [2] F. De Martino, G. Valente, N. Staeren, J. Ashburner, R. Goebel, and E. Formisano, "Combining multivariate voxel selection and support vector machines for mapping and classification of fmri spatial patterns," *Neuroimage*, vol. 43, no. 1, pp. 44–58, 2008.
- [3] M. Hanke, Y. O. Halchenko, P. B. Sederberg, S. J. Hanson, J. V. Haxby, and S. Pollmann, "Pymvpa: a python toolbox for multivariate pattern analysis of fmri data," *Neuroinformatics*, vol. 7, no. 1, pp. 37–53, 2009.
- [4] C. Habeck and Y. Stern, "Multivariate data analysis for neuroimaging data: overview and application to alzheimer's disease," *Cell biochemistry and biophysics*, vol. 58, no. 2, pp. 53–67, 2010.
- [5] C. Habeck, N. L. Foster, R. Perneczky, A. Kurz, P. Alexopoulos, R. A. Koeppel, A. Drzezga, and Y. Stern, "Multivariate and univariate neuroimaging biomarkers of alzheimer's disease," *Neuroimage*, vol. 40, no. 4, pp. 1503–1515, 2008.
- [6] G. L. Wenk *et al.*, "Neuropathologic changes in alzheimer's disease," *Journal of Clinical Psychiatry*, vol. 64, pp. 7–10, 2003.
- [7] G. Chételat, B. Desgranges, B. Landeau, F. Mezenge, J. Poline, V. de La Sayette, F. Viader, F. Eustache, and J.-C. Baron, "Direct voxel-based comparison between grey matter hypometabolism and atrophy in alzheimer's disease," *Brain*, vol. 131, no. 1, pp. 60–71, 2007.
- [8] L. G. Apostolova, C. A. Steiner, G. G. Akopyan, R. A. Dutton, K. M. Hayashi, A. W. Toga, J. L. Cummings, and P. M. Thompson, "Three-dimensional gray matter atrophy mapping in mild cognitive impairment and mild alzheimer disease," *Archives of neurology*, vol. 64, no. 10, pp. 1489–1495, 2007.
- [9] A. L. Janke, G. d. Zubicaray, S. E. Rose, M. Griffin, J. B. Chalk, and G. J. Galloway, "4d deformation modeling of cortical disease progression in alzheimer's dementia," *Magnetic Resonance in Medicine*, vol. 46, no. 4, pp. 661–666, 2001.
- [10] Z. Lao, D. Shen, Z. Xue, B. Karacali, S. M. Resnick, and C. Davatzikos, "Morphological classification of brains via high-dimensional shape transformations and machine learning methods," *Neuroimage*, vol. 21, no. 1, pp. 46–57, 2004.
- [11] C. Davatzikos, Y. Fan, X. Wu, D. Shen, and S. M. Resnick, "Detection of prodromal alzheimer's disease via pattern classification of magnetic resonance imaging," *Neurobiology of aging*, vol. 29, no. 4, pp. 514–523, 2008.

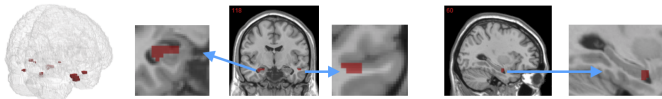


Fig. 11: The 2-d slice brain image of selected voxels with $2 \times 2 \times 2mm^3$ using coarse-to-fine approach.

believe that our methods can be extended to other applications.

- [12] R. Tibshirani, "Regression shrinkage and selection via the lasso," *Journal of the Royal Statistical Society. Series B (Methodological)*, vol. 58, pp. 267–288, 1996.
- [13] H. Zou and T. Hastie, "Regularization and variable selection via the elastic net," *Journal of the Royal Statistical Society: Series B (Statistical Methodology)*, vol. 67, no. 2, pp. 301–320, 2005.
- [14] M. Yuan and Y. Lin, "Model selection and estimation in regression with grouped variables," *Journal of the Royal Statistical Society: Series B (Statistical Methodology)*, vol. 68, no. 1, pp. 49–67, 2006.
- [15] L. Jacob, G. Obozinski, and J.-P. Vert, "Group lasso with overlap and graph lasso," in *Proceedings of the 26th annual international conference on machine learning*. ACM, 2009, pp. 433–440.
- [16] R. Jenatton, A. Gramfort, V. Michel, G. Obozinski, E. Eger, F. Bach, and B. Thirion, "Multiscale mining of fmri data with hierarchical structured sparsity," *SIAM Journal on Imaging Sciences*, vol. 5, no. 3, pp. 835–856, 2012.
- [17] N. Rao, C. Cox, R. Nowak, and T. T. Rogers, "Sparse overlapping sets lasso for multitask learning and its application to fmri analysis," in *Advances in neural information processing systems*, 2013, pp. 2202–2210.
- [18] V. Michel, A. Gramfort, G. Varoquaux, E. Eger, and B. Thirion, "Total variation regularization for fmri-based prediction of behavior," *IEEE transactions on medical imaging*, vol. 30, no. 7, pp. 1328–1340, 2011.
- [19] L. I. Rudin, S. Osher, and E. Fatemi, "Nonlinear total variation based noise removal algorithms," *Physica D: Nonlinear Phenomena*, vol. 60, no. 1–4, pp. 259–268, 1992.
- [20] A. Gramfort, B. Thirion, and G. Varoquaux, "Identifying predictive regions from fmri with tv-l1 prior," in *Pattern Recognition in Neuroimaging (PRNI), 2013 International Workshop on*. IEEE, 2013, pp. 17–20.
- [21] B. Xin, Y. Kawahara, Y. Wang, and W. Gao, "Efficient generalized fused lasso and its application to the diagnosis of alzheimer's disease," 2014.
- [22] G. E. P. Box, "Robustness in the strategy of scientific model building," *Robustness in Statistics*, pp. 201–236, 1979.
- [23] J. Ashburner and K. J. Friston, "Why voxel-based morphometry should be used," *NeuroImage*, vol. 14, no. 6, pp. 1238–1243, 2001.
- [24] B. Xin, L. Hu, Y. Wang, and W. Gao, "Stable feature selection from brain smri," *AAAI*, pp. 1910–1916, 2014.
- [25] A. E. Hoerl and R. W. Kennard, "Ridge regression: Biased estimation for nonorthogonal problems," *Technometrics*, vol. 12, no. 1, pp. 55–67, 1970.
- [26] L. Grosenick, B. Klingenberg, K. Katovich, B. Knutson, and J. E. Taylor, "Interpretable whole-brain prediction analysis with graphnet," *NeuroImage*, vol. 72, pp. 304–321, 2013.
- [27] C. Huang, X. Sun, J. Xiong, and Y. Yao, "Split lbi: An iterative regularization path with structural sparsity. advances in neural information processing systems," *Advances In Neural Information Processing Systems*, pp. 3369–3377, 2016.
- [28] G. B. Ye and X. Xie, "Split bregman method for large scale fused lasso," *Computational Statistics & Data Analysis*, vol. 55, no. 4, pp. 1552–1569, 2011.
- [29] W. Bo, S. Boyd, M. Annergren, and Y. Wang, "An admm algorithm for a class of total variation regularized estimation problems *," *Ifac Proceedings Volumes*, vol. 45, no. 16, pp. 83–88, 2012.
- [30] S. Osher, M. Burger, D. Goldfarb, J. Xu, and W. Yin, "An iterative regularization method for total variation-based image restoration," *Multiscale Modeling & Simulation*, vol. 4, no. 2, pp. 460–489, 2005.
- [31] S. Osher, F. Ruan, J. Xiong, Y. Yao, and W. Yin, "Sparse recovery via differential inclusions," *Applied and Computational Harmonic Analysis*, vol. 41, no. 2, pp. 436–469, 2016.
- [32] C. Huang and Y. Yao, "A unified dynamic approach to sparse model selection," *arXiv preprint arXiv:1810.03608*, 2018.
- [33] R. J. Tibshirani, J. E. Taylor, E. J. Candès, and T. Hastie, "The solution path of the generalized lasso," *The Annals of Statistics*, vol. 39, no. 3, pp. 1335–1371, 2011.
- [34] X. Sun, L. Hu, Y. Yao, and Y. Wang, "Gsplit lbi: Taming the procedural bias in neuroimaging for disease prediction," in *International Conference on Medical Image Computing and Computer-Assisted Intervention*. Springer, 2017, pp. 107–115.
- [35] A. Nemirovsky, "Problem complexity and method efficiency in optimization."
- [36] H. Braak and E. Braak, "Neuropathological staging of alzheimer-related changes," *Acta neuropathologica*, vol. 82, no. 4, pp. 239–259, 1991.
- [37] P. Visser, F. Verhey, P. Hofman, P. Scheltens, and J. Jolles, "Medial temporal lobe atrophy predicts alzheimer's disease in patients with minor cognitive impairment," *Journal of Neurology, Neurosurgery & Psychiatry*, vol. 72, no. 4, pp. 491–497, 2002.
- [38] B. Dubois, H. H. Feldman, C. Jacova, S. T. DeKosky, P. Barberger-Gateau, J. Cummings, A. Delacourte, D. Galasko, S. Gauthier, G. Jicha *et al.*, "Research criteria for the diagnosis of alzheimer's disease: revising the nincds–adrda criteria," *The Lancet Neurology*, vol. 6, no. 8, pp. 734–746, 2007.
- [39] S. Klöppel, A. Abdulkadir, C. R. Jack Jr, N. Koutsouleris, J. Mourão-Miranda, and P. Vemuri, "Diagnostic neuroimaging across diseases," *NeuroImage*, vol. 61, no. 2, pp. 457–463, 2012.
- [40] J. L. Whitwell, R. Avula, M. Senjem, K. Kantarci, S. Weigand, A. Samikoglu, H. Edmonson, P. Vemuri, D. S. Knopman, B. F. Boeve *et al.*, "Gray and white matter water diffusion in the syndromic variants of frontotemporal dementia," *Neurology*, vol. 74, no. 16, pp. 1279–1287, 2010.
- [41] A. L. Boxer, M. D. Geschwind, N. Belfor, M. L. Gorno-Tempini, G. F. Schauer, B. L. Miller, M. W. Weiner, and H. J. Rosen, "Patterns of brain atrophy that differentiate corticobasal degeneration syndrome from progressive supranuclear palsy," *Archives of neurology*, vol. 63, no. 1, pp. 81–86, 2006.
- [42] J. Xia, J. Miu, H. Ding, X. Wang, H. Chen, J. Wang, J. Wu, J. Zhao, H. Huang, and W. Tian, "Changes of brain gray matter structure in parkinson's disease patients with dementia," *Neural regeneration research*, vol. 8, no. 14, p. 1276, 2013.
- [43] J. Ashburner, "A fast diffeomorphic image registration algorithm," *NeuroImage*, vol. 38, no. 1, pp. 95–113, 2007.
- [44] K. M. Kennedy, K. I. Erickson, K. M. Rodrigue, M. W. Voss, S. J. Colcombe, A. F. Kramer, J. D. Acker, and N. Raz, "Age-related differences in regional brain volumes: a comparison of optimized voxel-based morphometry to manual volumetry," *Neurobiology of aging*, vol. 30, no. 10, pp. 1657–1676, 2009.
- [45] F. Duran, A. Valente, E. Miguel, C. Castro, and G. Busatto, "Risk of artifacts due to enlarged ventricles using voxel-based morphometry studies," *NeuroImage*, vol. 31, no. Suppl. 1, p. S45, 2006.
- [46] Y. Benjamini and Y. Hochberg, "Controlling the false discovery rate: a practical and powerful approach to multiple testing," *Journal of the Royal statistical society: series B (Methodological)*, vol. 57, no. 1, pp. 289–300, 1995.
- [47] B. Efron, "Local false discovery rates."
- [48] X. Sun, L. Hu, F. Zhang, Y. Yao, and Y. Wang, "Fdr-hs: An empirical bayesian identification of heterogenous features in neuroimage analysis," in *International Conference on Medical Image Computing and Computer-Assisted Intervention*. Springer, 2018, pp. 611–619.
- [49] M. Liu, D. Zhang, D. Shen, A. D. N. Initiative *et al.*, "Ensemble sparse classification of alzheimer's disease," *NeuroImage*, vol. 60, no. 2, pp. 1106–1116, 2012.
- [50] L. Wang, Y. Liu, H. Cheng, X. Zeng, and Z. Wang, "Elastic net based sparse feature learning and classification for alzheimer's disease identification," in *2017 39th Annual International Conference of the IEEE Engineering in Medicine and Biology Society (EMBC)*. IEEE, 2017, pp. 2288–2291.
- [51] Y.-K. Tu, M. Kellett, V. Clerehugh, and M. S. Gilthorpe, "Problems of correlations between explanatory variables in multiple regression analyses in the dental literature," *British dental journal*, vol. 199, no. 7, pp. 457–461, 2005.
- [52] M. Liu, D. Zhang, D. Shen, A. D. N. Initiative *et al.*, "Ensemble sparse classification of alzheimer's disease," *NeuroImage*, vol. 60, no. 2, pp. 1106–1116, 2012.
- [53] A. Beck and M. Teboulle, "Mirror descent and nonlinear projected subgradient methods for convex optimization," *Operations Research Letters*, vol. 31, no. 3, pp. 167–175, 2003.
- [54] W. Krichene, A. Bayen, and P. L. Bartlett, "Accelerated mirror descent in continuous and discrete time," in *Advances in neural information processing systems*, 2015, pp. 2845–2853.
- [55] S. Osher, F. Ruan, J. Xiong, Y. Yao, and W. Yin, "Sparse recovery via differential inclusions," *Applied and Computational Harmonic Analysis*, 2016.
- [56] J. Xiong, F. Ruan, and Y. Yao, "A tutorial on libra: R package for the linearized bregman algorithm in high dimensional statistics," *arXiv preprint arXiv:1604.05910*, 2016.
- [57] C. Huang, X. Sun, J. Xiong, and Y. Yao, "Boosting with structural sparsity: A differential inclusion approach," *Applied and Computational Harmonic Analysis*, 2018. [Online]. Available: <http://www.sciencedirect.com/science/article/pii/S1063520318300010>
- [58] A. Beck and M. Teboulle, "A fast iterative shrinkage-thresholding algorithm for linear inverse problems," *SIAM journal on imaging sciences*, vol. 2, no. 1, pp. 183–202, 2009.

- [59] J. Shi, W. Yin, and S. Osher, "A new regularization path for logistic regression via linearized bregman," *Rice CAAM Technical Report TR12-24*, 2012.
- [60] "A unified dynamic approach to sparse model selection," *Artificial Intelligence and Statistics*, 2018.
- [61] M. W. Weiner, P. S. Aisen, C. R. Jack, W. J. Jagust, J. Q. Trojanowski, L. Shaw, A. J. Saykin, J. C. Morris, N. Cairns, L. A. Beckett *et al.*, "The alzheimer's disease neuroimaging initiative: progress report and future plans," *Alzheimer's & Dementia*, vol. 6, no. 3, pp. 202–211, 2010.
- [62] Z. Dai, C. Yan, Z. Wang, J. Wang, M. Xia, K. Li, and Y. He, "Discriminative analysis of early alzheimer's disease using multi-modal imaging and multi-level characterization with multi-classifier," *Neuroimage*, vol. 59, no. 3, pp. 2187–2195, 2012.
- [63] L. R. Dice, "Measures of the amount of ecologic association between species," *Ecology*, vol. 26, no. 3, pp. 297–302, 1945.